

## Design and Testing of Aeroelastically Tailored Wings Under Maneuver Loading

Werter, Noud; Sodja, Jurij; De Breuker, Roeland

**DOI**

[10.2514/1.J054965](https://doi.org/10.2514/1.J054965)

**Publication date**

2016

**Document Version**

Accepted author manuscript

**Published in**

AIAA Journal: devoted to aerospace research and development

**Citation (APA)**

Werter, N., Sodja, J., & De Breuker, R. (2016). Design and Testing of Aeroelastically Tailored Wings Under Maneuver Loading. *AIAA Journal: devoted to aerospace research and development*, 55(3), 1012-1025. Advance online publication. <https://doi.org/10.2514/1.J054965>

**Important note**

To cite this publication, please use the final published version (if applicable). Please check the document version above.

**Copyright**

Other than for strictly personal use, it is not permitted to download, forward or distribute the text or part of it, without the consent of the author(s) and/or copyright holder(s), unless the work is under an open content license such as Creative Commons.

**Takedown policy**

Please contact us and provide details if you believe this document breaches copyrights. We will remove access to the work immediately and investigate your claim.

# Design and Testing of Aeroelastically Tailored Wings under Manoeuvre Loading\*

Noud P.M. Werter<sup>†</sup>, Jurij Sodja<sup>‡</sup> and Roeland De Breuker<sup>§</sup>

*Delft University of Technology, 2629 HS, Delft, the Netherlands*

The goal of the present paper is to provide experimental validation data for the aeroelastic analysis of composite aeroelastically tailored wings with a closed-cell cross-sectional structure. Several rectangular wings with different skin thicknesses and composite layups are designed in order to minimise root bending moment under manoeuvre loading using an aeroelastic analysis framework that closely couples a geometrically nonlinear beam model to a vortex lattice aerodynamic model. The globally convergent method of moving asymptotes is used to derive an optimised layup for the tailored wings. In addition a quasi-isotropic wing is analysed to serve as a reference. Both the tailored wings and the quasi-isotropic wing have been manufactured and tested structurally and in the wind tunnel. In the wind tunnel, aerodynamic forces and moments and wing deformation have been measured to provide experimental validation data.

---

\*Part of this work has been presented in Werter, N.P.M., Sodja, J., and De Breuker, R., 2015. Design and testing of an aeroelastically tailored wing under manoeuvre loadings. International Forum on Aeroelasticity and Structural Dynamics 2015, St. Petersburg, Russia. IFASD-2015-123

<sup>†</sup>PhD Candidate, Faculty of Aerospace Engineering, Kluyverweg 1, AIAA Member. n.p.m.werter@tudelft.nl

<sup>‡</sup>Researcher, Faculty of Aerospace Engineering, Kluyverweg 1, AIAA Member. j.sodja@tudelft.nl

<sup>§</sup>Assistant Professor, Faculty of Aerospace Engineering, Kluyverweg 1, AIAA Member. r.debreuker@tudelft.nl

## Nomenclature

$\mathbf{A}$	=	Laminate extensional stiffness matrix (N)
$e$	=	Shear center location relative to the chord with respect to the leading edge (-)
$\mathbf{C}$	=	Timoshenko cross-sectional stiffness matrix
$E_{11}$	=	Longitudinal stiffness (GPa)
$E_{22}$	=	Transverse stiffness (GPa)
$EI$	=	Bending stiffness ( $\text{Nm}^2$ )
$EI^*$	=	Effective bending stiffness ( $\text{Nm}^2$ )
$F$	=	Force ( $\text{N}^2$ )
$G_{12}$	=	Shear stiffness (GPa)
$GJ$	=	Torsional stiffness ( $\text{Nm}^2$ )
$GJ^*$	=	Effective torsional stiffness ( $\text{Nm}^2$ )
$K$	=	Bend-twist coupling stiffness ( $\text{Nm}^2$ )
$M$	=	Moment (Nm)
$t_{ply}$	=	Ply thickness (mm)
$V$	=	Flow speed (m/s)
$V_{i\mathbf{A}}$	=	In-plane lamination parameters
$V_{i\mathbf{B}}$	=	Coupling lamination parameters
$V_{i\mathbf{D}}$	=	Out-of-plane lamination parameters
$\bar{z}$	=	Normalized laminate thickness coordinate
$\alpha$	=	Angle of attack (deg)
$\gamma$	=	Shear strain (-)
$\epsilon$	=	Strain (-)
$\theta$	=	Ply angle (deg)
$\kappa$	=	Curvature (1/m)
$\nu_{12}$	=	Poisson's ratio (-)
$\rho$	=	Density ( $\text{kg/m}^3$ )
$\psi$	=	Non-dimensional bend-twist coupling (-)

## I. Introduction

Composite materials are gaining more and more interest in the aerospace industry. Composite materials have two main advantages: (i) they have favourable specific properties

compared to metals and (ii) their material properties can be tailored according to the structural needs. This second property allows for aeroelastic tailoring, which has been defined by Shirk et al.<sup>1</sup> as:

*the embodiment of directional stiffness into an aircraft structural design to control aeroelastic deformation, static or dynamic, in such a fashion as to affect the aerodynamic and structural performance of that aircraft in a beneficial way* (page 6)

Aeroelastic tailoring has been researched extensively over the years. A summary of early research on aeroelastic tailoring of swept and unswept wings has been written by Shirk et al.<sup>1</sup> More recently Qin et al.<sup>2,3</sup> have investigated the effect of aeroelastic tailoring on the aeroelastic instability of composite thin-walled beams. Furthermore, several papers on the use of aeroelastic tailoring in general and its potential benefits, have been written recently by Weisshaar.<sup>4-7</sup> More specifically, research has been done on the use of aeroelastic tailoring in order to minimize structural weight,<sup>8-11</sup> maximize flutter speed,<sup>10,12-15</sup> optimize the gust response characteristics of the wings,<sup>16</sup> or the effect of tow-steered composites on wing aeroelastic characteristics.<sup>17,18</sup> Several researchers<sup>19-21</sup> have used a gradient-based optimiser with adjoint sensitivities to achieve aeroelastic tailoring by optimising a combination of laminate thickness and the fraction of 0 deg, 45 deg, -45 deg, and 90 deg plies in the stacking sequence. An example of the use of aeroelastic tailoring in non-aerospace applications is the research by Thuwis et al.<sup>22</sup> on the use of aeroelastic tailoring on the rear wing of a F1 car.

As can be seen, substantial research is done on the potential benefits of aeroelastic tailoring; however, little experimental validation data is available. Sherrer et al.<sup>23</sup> investigated the effect of aeroelastic tailoring on the divergence speeds using several composite plates at various sweep angles. Similar tests were carried out by Blair and Weisshaar<sup>24</sup> investigating the effect of ply angle on the divergence speed of a wing at different sweep angles, by varying the ply orientation of a composite plate covered by an aerodynamic fairing. Following this work, Dugundji and co-workers<sup>25-27</sup> performed several sets of experiments investigating the effect of aeroelastic tailoring on the divergence speed, flutter speed, and wing tip deflection of composite plates both cantilevered and with rigid-body-freedom.

Although these studies provide valuable experimental validation data, they are unsuitable for the validation of aeroelastic analysis frameworks that use a closed-cell cross-sectional structure (e.g. a wingbox) as design space for aeroelastic tailoring. These structures use the extension-shear coupling of the individual laminates of the wing cross-section to obtain bend-twist coupling at a wing level, while in a plate structure, the bend-twist coupling originates from the bend-twist coupling of the laminate. Therefore the goal of the present paper is to provide experimental validation data for the aeroelastic analysis of composite aeroelastically

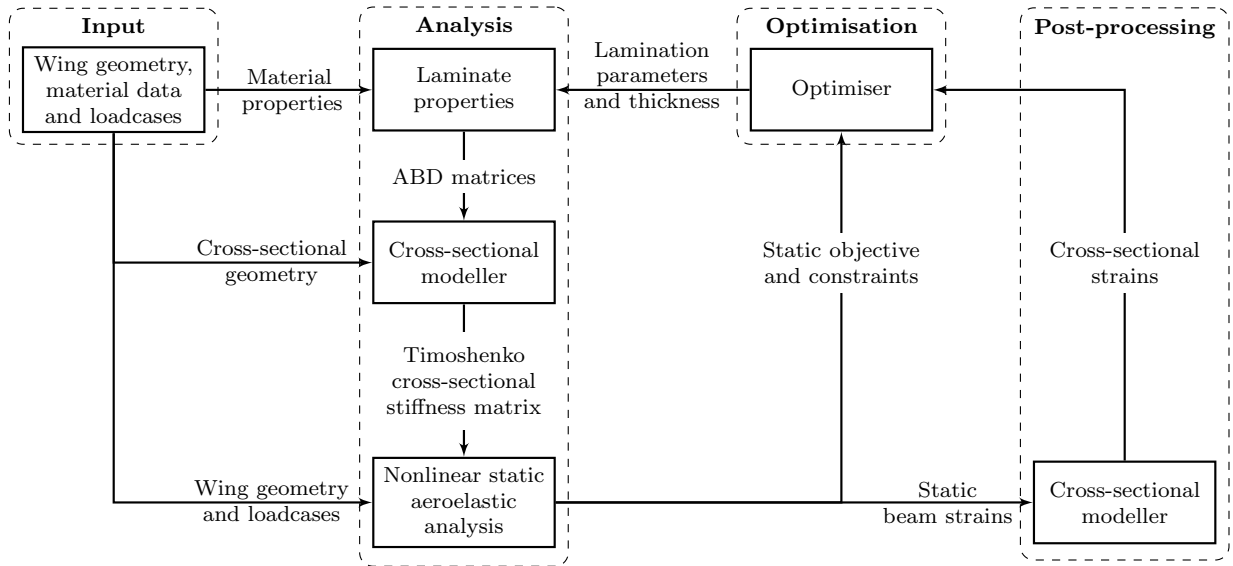


Figure 1: Static aeroelastic analysis framework

tailored wings with a closed-cell cross-sectional structure.

First, an overview of the aeroelastic analysis module used to analyse and design the aeroelastically tailored wings is given in section II, followed by an explanation of the optimisation procedure used to design the wings in section III. The optimisation results and the actual wing designs are presented in section IV. Section V presents the wing manufacturing process and the experimental setup. Finally, the experimental results are compared to the numerical results in section VI, followed by the conclusions in section VII.

## II. Aeroelastic Analysis Module

This section provides an overview of the static aeroelastic analysis that was used to analyse the aeroelastic performance of the composite wing considered. For a more detailed description of the different components, the reader is referred to Werter and De Breuker.<sup>28</sup> The purpose of the aeroelastic analysis and optimisation framework is to analyse and design conventional wingbox structures with ribs, spars, stringers, and a load bearing skin or, in case of the experimental wings considered in this paper, wings with only a load bearing outer skin. Fig. 1 shows a schematic overview of the static aeroelastic analysis and the different modules it consists of.

First, the three-dimensional wing geometry is split in several spanwise sections, where each spanwise section can have several laminates throughout the cross-section of the wing, as selected by the user. Instead of describing the composite laminates by ply angles and a stacking sequence to obtain the stiffness properties, each laminate is described by lamination parameters and the laminate thickness, resulting in a fixed number of continuous design

variables per laminate. Lamination parameters were first introduced by Tsai and Pagano<sup>29</sup> and provide a representation of a composite laminate as an integrated form. This way, the number of design variables is reduced and a gradient-based optimiser can be used to allow for a more efficient exploration of the composite design space.

The aeroelastic analysis and optimisation loop starts with the definition of the material properties, wing geometry and load cases as inputs. Next, using the material properties defined as input and the lamination parameters and laminate thickness generated by the optimiser, the properties of each of the laminates is computed. In order to generate the beam model, these laminate properties, together with the cross-sectional geometry, are used to generate the Timoshenko cross-sectional stiffness matrix with respect to the beam reference axis using the cross-sectional modeller developed by Ferede et al.<sup>30</sup> The cross-sectional modeller discretizes the cross-section using linear Hermitian shell elements to obtain the Timoshenko cross-sectional stiffness matrix of any arbitrary, open or closed, thin-walled composite cross-section including any possible spars and stringers.

As a third step, a geometrically nonlinear static aeroelastic analysis is carried out to obtain the nonlinear static displacement field of the aircraft for the various load cases. The static aeroelastic analysis model monolithically couples a geometrically nonlinear Timoshenko beam model based on the co-rotational formulation to an aerodynamic model based on the vortex lattice method. The vortex lattice method is based on potential flow theory and a thin wing approximation is made by modelling the wing by its camber surface. Both models are closely coupled and a geometrically nonlinear aeroelastic solution is obtained by using load control and the Newton-Raphson root finding method. A geometrically nonlinear model was used to account for the effects of large deformation on the aeroelastic performance of aircraft wings, since aeroelastic tailoring in general results in more flexible wing structures that might show geometric nonlinearity, while the use of a beam model ensures a computationally efficient model suitable for optimisation. The effect of the warping restraint at the wing root on the structural deformations is not accounted for; however, this effect is considered negligible for slender beam structures. All analyses are performed at a trimmed flight condition by adjusting the angle of attack such that lift equals weight, in order to compare the structural performance of the wings under equivalent aerodynamic loads.

Finally, in the fourth module, the analysis results are processed and the output is generated. The module provides the deformed wing geometry and aeroelastic loads. Furthermore, the cross-sectional modeller can be used to compute the skin strains from the beam deformations and, as such, assess the structural performance of the wing. Future work on the model includes the introduction of a skin buckling constraint to ensure buckling free designs.

**Table 1: Experimental wing geometry**

Semispan (m)	1.0
Chord (m)	0.2
Aspect ratio (-)	10
Sweep angle (deg)	0
Taper ratio (-)	1
Airfoil	NACA0012

### III. Optimisation Setup

In order to find designs that can be used for experimental validation and in the process show potential benefits of aeroelastic tailoring for manoeuvre load alleviation, several optimisations were carried out. In order to test a wing that would fit in the wind tunnel and can serve as validation for the aeroelastic framework, a rectangular wing with a semispan of 1.0 m and an aspect ratio of 10 was selected, resulting in the wing dimensions given in Table 1. Wing designs were created for two different cases, quasi isotropic (QI) and aeroelastically tailored.

The objective of the optimisation is to minimise the maximum root bending moment of the wing for several manoeuvre load conditions, as defined in Table 2. Constraints were put on the maximum skin strains (see Table 3), the trim angle of attack ( $\leq 10$  deg), and the lamination parameters to ensure a feasible structural design and a valid aerodynamic response. For manufacturing purposes, the optimisation was set up such that all composite laminates have a fixed skin thickness and their layup is symmetric to prevent any warping upon curing. As mentioned in Section II, the composite laminates are described by lamination parameters. They are related to the ply angles and stacking sequence through the following relations:

$$(V_{1A}, V_{2A}, V_{3A}, V_{4A}) = \int_{-1/2}^{1/2} (\cos 2\theta, \sin 2\theta, \cos 4\theta, \sin 4\theta) d\bar{z} \quad (1)$$

$$(V_{1B}, V_{2B}, V_{3B}, V_{4B}) = 4 \int_{-1/2}^{1/2} \bar{z} (\cos 2\theta, \sin 2\theta, \cos 4\theta, \sin 4\theta) d\bar{z} \quad (2)$$

$$(V_{1D}, V_{2D}, V_{3D}, V_{4D}) = 12 \int_{-1/2}^{1/2} \bar{z}^2 (\cos 2\theta, \sin 2\theta, \cos 4\theta, \sin 4\theta) d\bar{z} \quad (3)$$

**Table 2: Manoeuvre load cases**

Load case	#1	#2	#3
Flight speed (m/s)	100	100	100
Mach Number	0.29	0.29	0.29
Density (kg/m <sup>3</sup> )	1.225	1.225	1.225
Load factor (-)	1	2.5	-1
Aircraft mass (kg)	56	56	56
Half wing lift (N)	274.7	686.7	-274.7

where  $V_{\mathbf{A}}$ ,  $V_{\mathbf{B}}$ , and  $V_{\mathbf{D}}$  are the in-plane, coupling, and bending lamination parameters and  $\bar{z}$  is the normalised through-the-thickness coordinate. In order to ensure a feasible design, Hammer et al.<sup>31</sup> derived a set of closed form expressions that define the feasible region of the in-plane, coupling, and bending lamination parameters separately, given by:

$$2V_1^2(1 - V_3) + 2V_2^2(1 + V_3) + V_3^2 + V_4^2 - 4V_1V_2V_4 \leq 1 \quad (4)$$

$$V_1^2 + V_2^2 \leq 1 \quad (5)$$

$$-1 \leq V_i \leq 1 \quad (6)$$

The use of lamination parameters as design variables describing the stiffness properties of a laminate has several advantages over the use of ply angles and a stacking sequence, especially for optimisation. Optimisation of laminated composite structures through ply angles and a stacking sequence requires an optimiser suitable for discrete design variables due to the discrete ply thickness of the laminates and the discrete ply angles commonly used in production processes. Lamination parameters, on the other hand, provide a continuous description of composite laminates, allowing for more efficient gradient-based optimisers to be used. Secondly, any composite laminate is described by a fixed number of 12 lamination parameters and its thickness, while in the case of ply angles and a stacking sequence, the number of design variables scales with the number of plies in the laminate, making optimisation more difficult as the size of the laminate grows. In case of the present design optimisation, for a symmetric laminate with a prescribed thickness, where the laminate in-plane properties are dominant for the response, this results in 4 design variables,  $V_{1\mathbf{A}} - V_{4\mathbf{A}}$ , per laminate. Finally, the use of lamination parameters results in a smoother design space, while the design space in fibre angle space is highly irregular due to the highly nonlinear relation between the laminate stiffness matrices and the ply angles.

Note that, the disadvantage of lamination parameters is that they only provide a theo-

**Table 3: Material properties**

Material	CYCOM 977-2-35 12k HTS	CYCOM 977-2-35 12k HTS (Fibre volume corrected)	Epoxy resin	EPP Foam
$E_{11}$ (GPa)	125.93*	142.70	2.90	$9.8 \cdot 10^{-3}$
$E_{22}$ (GPa)	7.72*	8.72	2.90	$9.8 \cdot 10^{-3}$
$G_{12}$ (GPa)	3.61 <sup>†</sup>	4.38	1.07	$3.77 \cdot 10^{-3\ddagger}$
$\nu_{12}$ (-)	0.336*	0.336	0.35	0.3 <sup>§</sup>
$\rho$ (kg/m <sup>3</sup> )	1590	1620	1150	20
$t_{ply}$ (mm)	0.26	0.23	-	-
$V_f$ (-)	0.60	0.68	-	-
$\epsilon_{x_{max}}$ ( $\mu$ strain)	4500 <sup>¶</sup>	-	-	-
$\gamma_{max}$ ( $\mu$ strain)	7000 <sup>¶</sup>	-	-	-

\* according to ASTM Standard D3039

<sup>†</sup> according to ASTM Standard D3518

<sup>‡</sup> according to  $G = \frac{E}{2(1+\nu)}$

<sup>§</sup> assumed

<sup>¶</sup> includes knockdown factors for environmental effects and material scatter

retical optimum as they can only be matched exactly by an infinite number of layers. Some loss in performance of the wing is to be expected when these lamination parameters are converted to an actual laminate; however, the optimisation provides a good starting point to find the actual laminates that provide optimal performance. The sensitivities of the objective and constraints to the lamination parameters are computed analytically and the globally convergent method of moving asymptotes<sup>32</sup> was used as the optimiser.

The quasi isotropic wing was built and analysed as a reference to be able to assess the potential benefits of the tailored wing. The tailored wing consists of two independent laminates that are constant along the span: one for the top skin and one for the bottom skin, resulting in a total of 8 design variables.

## IV. Design of the Wings

Using the described optimisation setup, several tailored wings with different skin thickness were designed, as is described in section A. Based on these optimisation results, two wings were built, as described in section B.

## A. Optimisation results

The wings are made out of CYCOM 977-2-35 12k HTS carbon fibre epoxy with material properties as given in Table 3. Initially a tailored wing with a skin thickness of 3 layers was optimised to obtain a flexible wing with potential for aeroelastic tailoring. As expected, the critical load case for the wing was the 2.5g manoeuvre load, hence analysis results are only presented for this load case. Since no quasi-isotropic layup exists for a 3 layer wing, the performance of the optimised 3 layer wing has been compared to an equivalent quasi-isotropic set of lamination parameters with the same thickness. When performing structural tests, the 3 layer tailored skin buckled and was unsuitable for further testing. Therefore, another design was created for a 4 layer tailored wing that was designed and manufactured based on the experience gained with the 3 layer tailored wing and the 6 layer quasi-isotropic wing. The optimum lamination parameters are given in Table 4 and the resulting root bending moments are given in Table 5. Note that the trim weight for all wings is based on an aircraft mass of 56 kg at 1g flight, resulting in similar root bending moments for all skin thicknesses.

**Table 4: Optimum lamination parameters**

	3 Layers		4 Layers	
	Top skin	Bottom skin	Top skin	Bottom skin
$V_{1A}$	0.282	0.283	0.382	0.290
$V_{2A}$	0.500	0.520	0.521	0.578
$V_{3A}$	0.395	0.341	0.409	0.310
$V_{4A}$	0.457	0.435	0.631	0.489

**Table 5: Root bending moment results for the 2.5g load case for the optimised and actual laminates**

Wing type		Root bending moment (Nm)			
		Optimised		Actual Laminates	
6 layers	QI	317.2		317.2	
4 layers	QI	317.3		317.3	
	Tailored	290.0	-8.58%	290.8	-8.34%
3 layers	QI	317.3		317.3	
	Tailored	290.6	-8.43%	292.6	-7.80%

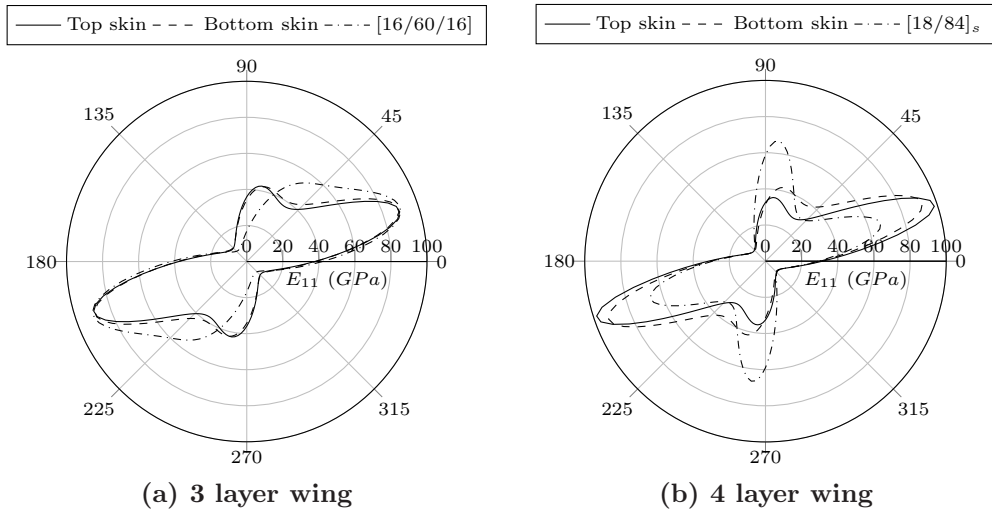


**Figure 2: Comparison of the extensional stiffness in different directions between the optimised results and the corresponding laminates. The 0 deg fibres are oriented along the wing axis and a layer with a positive angle is oriented forward.**

## B. Final wing designs

The result of the optimisation is a set of lamination parameters. In order to find a corresponding laminate that can be manufactured, a sweep over the ply angles was done to find the laminate that best matches the stiffness properties obtained using the optimum lamination parameters. In order to evaluate the match between the stacking sequence and the optimised lamination parameters, the directional stiffness of the laminates is visualised by computing the modulus of elasticity along a direction,  $\theta$ , from the laminate extensional stiffness matrix,  $\mathbf{A}$ , obtained from classical lamination theory, as introduced by Dillinger et al.<sup>11</sup> The modulus of elasticity of a laminate along an axis rotated with an angle,  $\theta$ , with respect to the laminate axis is defined by:

$$E_{11}(\theta) = \frac{1}{A_{11}^{-1}(\theta)} \quad (7)$$

where

$$A_{11}^{-1}(\theta) = T^T A_{11}^{-1} T \quad (8)$$

and

$$T = \begin{bmatrix} \cos^2(\theta) & \sin^2(\theta) & 2 \cos(\theta) \sin(\theta) \\ \sin^2(\theta) & \cos^2(\theta) & -2 \cos(\theta) \sin(\theta) \\ -\cos(\theta) \sin(\theta) & \cos(\theta) \sin(\theta) & \cos^2(\theta) - \sin^2(\theta) \end{bmatrix} \quad (9)$$

**Table 6: Wing laminates where the ply angle is defined positive with respect to the wing axis when the fibres are oriented forward when going from root to tip**

Wing type		Laminate
6 layers	QI	$[60/0/ - 60]_s$
4 layers	Tailored	$[18/84]_s$
3 layers	Tailored	$[16/60/16]$

The resulting stiffness distributions of both the optimised laminates and the retrieved stacking sequences are shown in Figure 2a and Fig. 2b for the 3 layer and 4 layer wing respectively. As can be seen, the stiffness distributions for the top and bottom skins are very similar, so, for ease of manufacturing, it was decided to select the same laminate for the top and bottom skins, resulting in a symmetric wing about the chord.

As can be concluded from Fig. 2, upon converting from lamination parameters to an actual stacking sequence, a trade-off needs to be made to find the stacking sequence that best matches the lamination parameter optimum. In case of the 3 layer wing, this results in a stacking sequence that accurately captures the main stiffness direction by means of the 16 deg plies, however, at a reduced performance along the second stiffness direction, since only one additional ply is available. In case of the 4 layer wing, the restriction of a symmetric laminate results in a laminate with two ply directions with two plies per direction. As can be seen, this results in a stacking sequence that captures the two main stiffness directions; however, the ratio in stiffness between these two directions cannot be captured by the stacking sequence. As expected, some performance is lost due to the transformation of lamination parameters to actual ply orientations, as can be seen in Table 5. The actual laminates, however, still show a clear benefit of aeroelastic tailoring for manoeuvre load reduction. The corresponding laminates can be found in Table 6.

Wash-out bend-twist coupling is introduced by orienting the fibres forward with respect to the wing axis, thus shifting the spanwise center of pressure inboard. Note that the bend-twist coupling on a wing level is not introduced by bend-twist coupling of the laminates, but by extension-shear coupling instead. Under bending, one skin will be in compression, while the other skin will be in tension, and, consequently both skins will shear in opposite direction. By constraining the relative shear deformation between individual skins, wing twist is introduced.

In order to prevent flattening of the cross-section under deflection, four equally spaced EPP foam ribs (the material properties can be found in Table 3) with a width of 20mm were installed as cross-sectional reinforcements in the 3 and 6 layer wings. Despite locally supporting the skins, the 3 layer wing buckled during the structural test and was discarded

**Table 7: Buckling load and tip deflection for various wing core configurations for a 4 layer tailored skin**

Case	No ribs	Rib spacing 10 cm	Full core
Static load (N)	200	200	200
Buckling load (N)	83.8	101.5	797.4
Tip deflection (mm)	67.7	67.5	64.8
Tip twist (deg)	5.19	5.17	4.81

from further testing. As mentioned, a 4 layer tailored wing was designed instead. In order to prevent the 4 layer wing from buckling, a FEM buckling analysis was done in ABAQUS with an equivalent tip load of 200 N at the quarter chord to simulate a similar deflection and chordwise load introduction as anticipated in the wind tunnel experiments. The resulting wing tip deflection, tip twist, and buckling loads are presented in Table 7. For a rib spacing of 10 cm the EPP foam ribs still do not provide sufficient support to prevent skin buckling and, therefore, the 4 layer wings were completely filled with EPP foam, resulting in sufficient resistance to buckling, while only reducing the expected tip deflection by 4.3% and the expected tip twist by 7.3%.

## V. Manufacturing and experimental setup

As presented in section B, three wings were designed: a 3 layer tailored wing, a 4 layer tailored wing, and a 6 layer quasi-isotropic wing. The manufacturing process and the experimental setup are presented in more detail in the following sections.

### A. Manufacturing

In order to ensure high geometrical accuracy and high quality surface finish, the wings were manufactured using a hand-layup moulding technique. Since unidirectional carbon fibre prepreg is used that has to be cured in the autoclave at elevated temperature and pressure, a female mould was CNC milled out of aluminium.

The manufacturing procedure consists of the following steps. First the prepreg tape is cut using a cutting robot into quadrilateral patches according to individual ply-orientation requirements. This way the different plies can be easily oriented in the mould and the correct orientation of the fibres in the layup is ensured. After all the material has been stacked into the mould, the acquired layup is vacuum-bagged and cured in the autoclave. The cured skins are then trimmed down to final size, and the skin thickness is measured and used as an offset for manufacturing the EPP ribs and core. The EPP foam was cut using a CNC

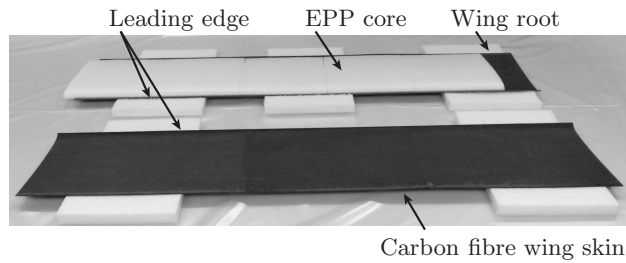


**Figure 3: Wing components before assembly**



**Figure 4: Vacuum bagging of the assembled wings to ensure proper bonding of both wing halves**

hot-wire cutting machine. The ribs and core are glued into the wing by means of epoxy. In order to connect the two wing halves, a strip of carbon fibre weave at an orientation of  $\pm 45$  deg is glued in the leading edge on both the inside and the outside of the wing in order to transfer the loads. At the trailing edge, because of the larger contact surface, the wings are glued together by means of epoxy. Once the wing components are assembled, the wing is placed in the mould, packed in a vacuum bag and kept under vacuum as the epoxy cures, in order to ensure good bonding. Fig. 3 and 4 show the individual components before final assembly and the assembled wing in the vacuum bag.

## B. Structural test setup

As a first comparison between the experimental wings and the simulation results, two series of structural tests were carried out. The objective of these tests is twofold: (i) provide initial validation data for the numerical model and (ii) assess the importance of features in the experimental wings (e.g. the EPP foam and reinforcements for bonding) that are not included in the numerical model.

First, each wing has been subjected to a load at 97.5% span introduced by a mass of up to 10 kg at different chordwise locations in order to validate the structural model. Fig. 5 shows a picture of the load introduction during the structural tests. The wing deformation is measured by a VIC3D stereo digital image correlation (DIC) system<sup>33</sup> yielding the 3D deformation field of the entire wing surface with a measurement accuracy of 0.1 – 0.2 mm.

Secondly, based on the comparison between the numerical model and the structural test results, an extra structural test was carried out for the 4 layer tailored wing subject to a pure torque of up to 20 Nm introduced through a cable and pulley system, such that the wing tip is free to deflect. This test fully decouples the torsional stiffness and bend-twist

**Table 8: Laser measurement characteristics**

Sensor position		Sensor range (mm)	Sensor resolution (mm)
Spanwise (mm)	Chordwise w.r.t. LE (mm)		
258 (25.8% span)	60 (30.0% chord)	20	$\pm 0.004$
258 (25.8% span)	185 (92.5% chord)	20	$\pm 0.004$
558 (55.8% span)	60 (30.0% chord)	50	$\pm 0.01$
558 (55.8% span)	185 (92.5% chord)	50	$\pm 0.01$
858 (85.8% span)	60 (30.0% chord)	100	$\pm 0.02$
858 (85.8% span)	185 (92.5% chord)	100	$\pm 0.02$

**Figure 5: Picture of the structural test setup illustrating an applied tip torque**

coupling of the wing from the shear center location and bending stiffness, resulting in a better structural characterisation of the 4 layer tailored wing. Since the anticipated deflections are in the range of 0.4 – 5 mm, the resolution of the VIC3D system is no longer sufficient and Micro-Epsilon optoNCDT 1302 laser distance sensors<sup>34</sup> were used to measure deformations. The sensors were positioned in pairs at three different spanwise locations, as defined in Table 8.

### C. Wind tunnel test setup

The wings were tested in the low turbulence wind tunnel (LTT) of the Delft University of Technology, which has an octagonal cross-section of 1.80 m by 1.25 m and a maximum wind speed of 120 m/s. The 4 layer tailored wing and the 6 layer quasi-isotropic wing have been tested at a range of angles of attack from  $-10$  deg to  $10$  deg at wind tunnel speeds up to 80 m/s up until wing buckling. The aerodynamic forces and moments were measured by the mechanical six-component balance present in the wind tunnel.

Wing deformation was measured by two independent methods: a VIC3D DIC system and

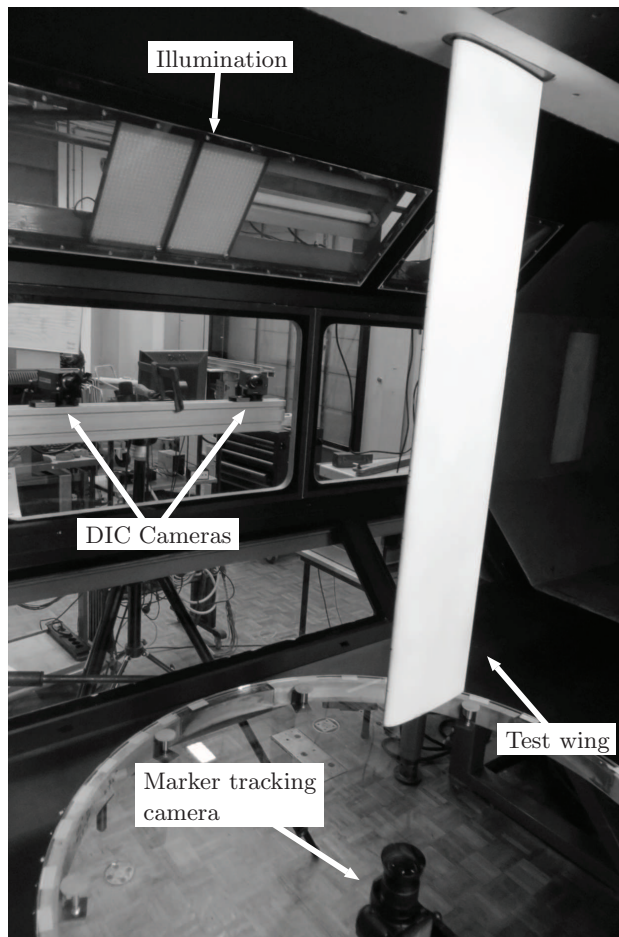


**Figure 6: Wind tunnel test setup**

an optical marker tracking system. The wind tunnel test setup is shown in Fig. 6. Optical marker tracking was carried out using a camera oriented along the span axis observing the wing tip. A set of distinctive markers was placed on the wing tip and were photographed during the experiment. In post-processing, the displacement of the markers is used to track the displacement and twist of the wing tip. The accuracy of the optical marker tracking system is  $\pm 0.05$  mm. A set of captured frames with the recognized markers is shown in Fig. 7. The position and orientation of the camera with respect to the wing is shown in Fig. 6.

## VI. Results

Detailed numerical and experimental results are presented for the 6 layer quasi-isotropic wing and for the 4 layer tailored wing. In the remainder of the paper, these wings are referred to as QI and tailored. All numerical results are obtained using the retrieved stacking sequences given in Table 6. First, the structural test results will be presented, followed by the aerodynamic and aeroelastic results obtained in the wind tunnel.

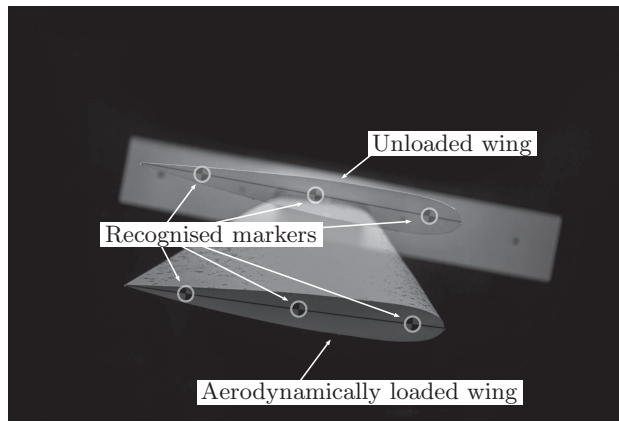


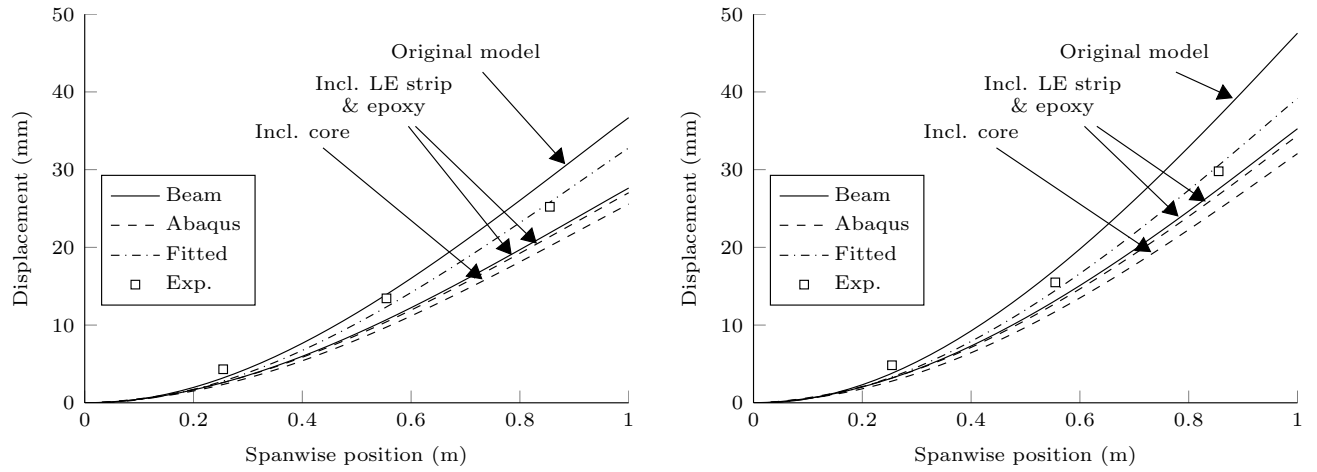
**Figure 7:** Overlay of tip photos of the unloaded and loaded 4 layer tailored wing at  $\alpha = 10$  deg and  $V = 80$  m/s

### A. Structural test

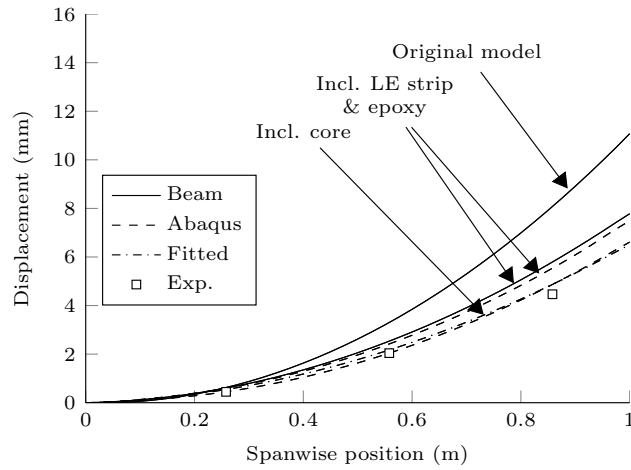
In the structural tests, the wings were first subjected to a load at 97.5% span at different chordwise locations. The load has been applied by masses in steps of 2 kg up to 10 kg. In order to reduce the effect of measurement errors, a load-displacement curve is created for each of the measurement series and the stiffness of the wing to a specific load case is determined by means of a linear least-squares fit. This way, a single parameter is obtained for each load case that is used to compare the results of the structural test to the simulations.

The wing out-of-plane displacement and wing twist results of the structural tests are shown in Fig. 8 and Fig. 9 for the tailored wing, and Fig. 10 and Fig. 11 for the QI wing, respectively. As can be seen, the original numerical beam model predicts a more flexible wing than found in the experiment. In order to investigate the sources of discrepancy between the numerical beam model and the experimental wing, the tailored wing was cut to inspect the interior of the wing, as shown in Fig. 12. Upon investigation of the geometry of the experimental wing and the mould, a first source of discrepancy was found in the wing geometry, as illustrated in Fig. 13.

A second source of discrepancy was identified by comparing the experimental wing to the test samples that have been used at the TU Delft to identify the material properties. While the material test samples had a ply thickness of 0.26 mm, the experimental wing has a ply thickness of 0.23 mm instead of the expected 0.26 mm. This discrepancy can be explained by the difference in the manufacturing process between both the experimental wing and the material test samples. Even though, both were manufactured using the same batch of material and under the same curing cycle, the material test samples were supported by an aluminium plate on the top and bottom, while the experimental wing skin was only supported by the mould on its outer surface and had a breather mesh on its inner surface, resulting in a loss of resin into the breather mesh during curing. Under the assumption of



(a) 10 kg load at 97.5% span at the leading edge      (b) 10 kg load at 97.5% span at the trailing edge



(c) Torque of 20 Nm

Figure 8: Comparison of the wing displacement of the tailored wing between the beam model, Abaqus, and the experiments

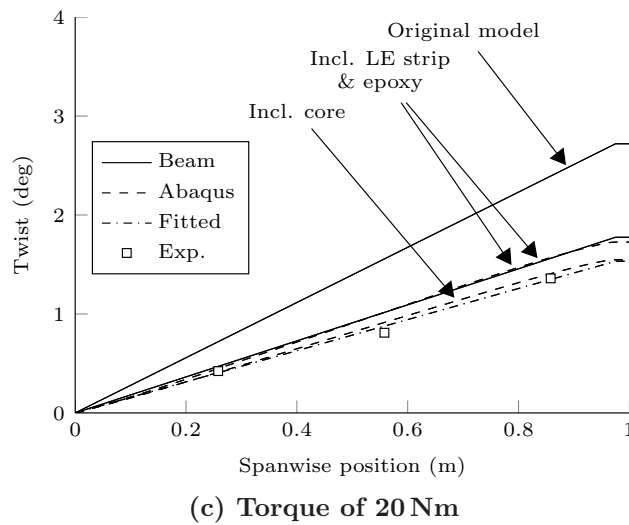
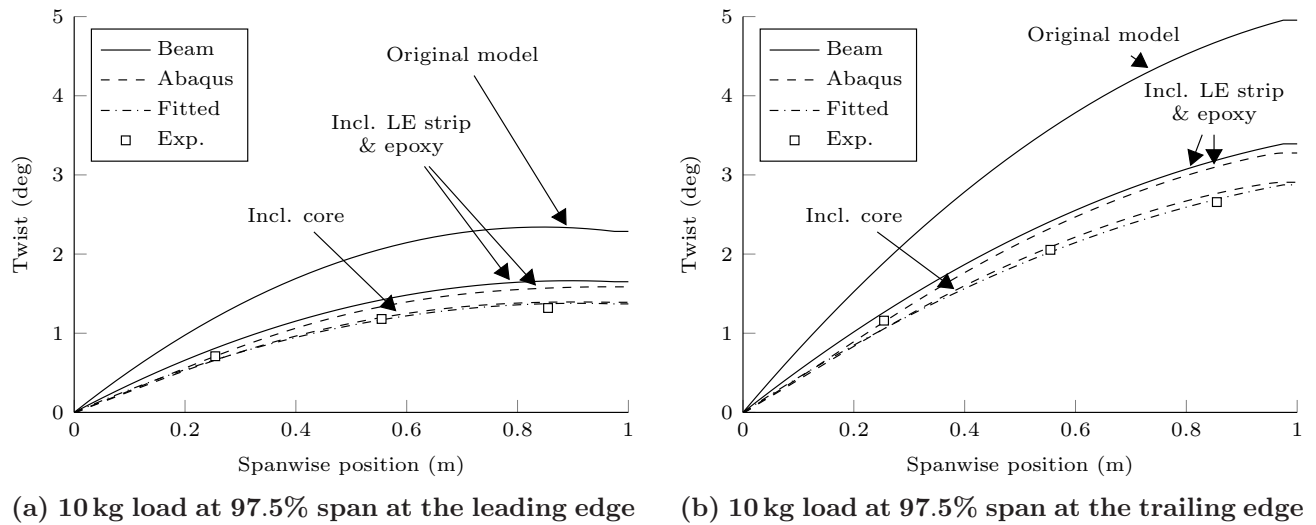


Figure 9: Comparison of the wing twist of the tailored wing between the beam model, Abaqus, and the experiments

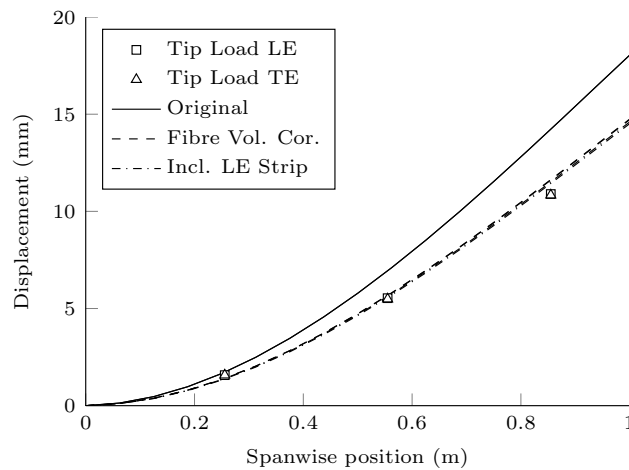


Figure 10: Wing displacement of the QI wing under a leading edge and trailing edge load at 97.5% span

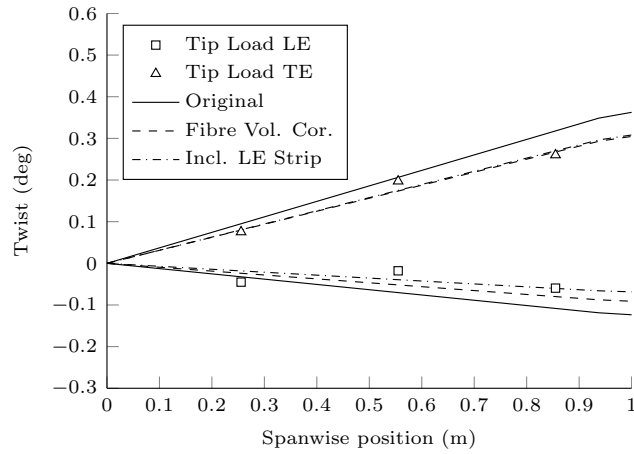


Figure 11: Wing twist of the QI wing under a leading edge and trailing edge load at 97.5% span



Figure 12: Cross-section of the experimental wing

equal fibre content per ply between both sets, this results in an increase in fibre volume fraction from 0.6 for the material test samples to 0.68 for the experimental wing. Using the rule of mixtures<sup>35</sup> to estimate the change in material properties, this results in the fibre volume corrected properties as shown in Table 3.

Thirdly, as can be seen in Fig. 12, three different regions on the wing surface can be identified and have to be accounted for: (i) the wing skin reinforced on the inside and outside with a strip of carbon fibre weave of 0.56 mm thickness for the first 2.5 mm oriented at  $\pm 45$  deg, (ii) the wing skin reinforced only on the inside with a strip of carbon fibre weave of 0.56 mm thickness from 2.5 mm to 24 mm oriented at  $\pm 45$  deg, and (iii) the remainder of the wing skin reinforced with a layer of 0.1 mm epoxy.

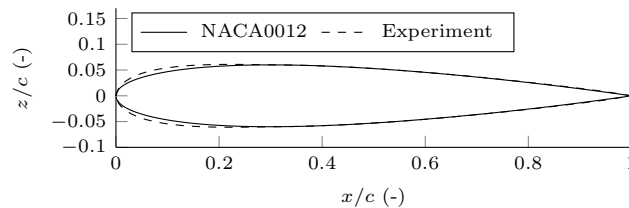


Figure 13: Comparison between the NACA0012 and the airfoil of the experimental wings

Based on these discrepancies, the airfoil geometry, material properties, and laminates have been updated to account for these effects, resulting in the additional beam results in Fig. 8-11. As shown in Fig. 10 and Fig. 11, the updated simulation results of the QI wing show excellent agreement with the experimental results; however, as shown in Fig. 8 and Fig. 9, the updated simulation results of the tailored wing still show significant discrepancies in both wing displacement and wing twist. In order to investigate this in more detail, as mentioned in section B, a second series of structural tests has been carried out on the tailored wing under a pure tip torque to decouple the torsional stiffness and bend-twist coupling of the wing from the shear center location and bending stiffness. The torque has been applied by a simultaneous upward force at the leading edge and an equivalent downward force at the trailing edge at 97.5% span in steps of 2 kg up to 10 kg, resulting in a maximum tip torque of 20 Nm. Similar to the applied load, a linear fit through the load displacement curve is used to obtain a single parameter to compare to the simulations. As can be seen in Fig. 8c and Fig. 9c, the simulations also show discrepancies in wing displacement and wing twist for an applied tip torque.

Based on the structural test results, it was decided to do a structural characterisation of the tailored wing by finding the equivalent bending stiffness, torsional stiffness, bend-twist coupling and shear center location that provide a best fit to the structural test results. For this purpose, an optimisation is set up with minimising the root mean squared error between the numerical beam simulations and the structural test results as objective. The errors are normalised with respect to the maximum displacement or twist of the corresponding loadcase, in order to weigh each measurement equally.

Consider the Timoshenko cross-sectional stiffness matrix, relating the cross-sectional forces to the cross-sectional strains:

$$(F_1, F_2, F_3, M_1, M_2, M_3)^T = \mathbf{C}(\epsilon_{11}, \epsilon_{12}, \epsilon_{13}, \kappa_1, \kappa_2, \kappa_3)^T \quad (10)$$

In case of slender composite beams loaded in bending and twist, not all components of the Timoshenko cross-sectional stiffness have a significant impact on the resulting deformations. The extensional and shear deformations are small and, therefore, the deformations of the beam are mainly governed by the bending stiffness, torsional stiffness, bend-twist coupling and shear center location. These are related to the components of the Timoshenko cross-sectional stiffness and compliance ( $\mathbf{C}^{-1}$ ) matrix through the following relations:

$$EI = C_{55} \quad (11)$$

$$GJ = C_{44} \quad (12)$$

$$K = -C_{45} \quad (13)$$

$$e = -\frac{C_{34}^{-1}}{C_{44}^{-1}} \quad (14)$$

The results of the fitting process for these parameters are given in the final column of Table 9 and the corresponding match to the structural deformations is shown Fig. 8 and Fig. 9.

**Table 9: Effect of different components of the experimental tailored wing on its stiffness. The last column shows the differences between the experimental properties, and the updated beam and the Abaqus model including core, respectively.**

Property		Fibre volume corrected	Incl. LE strips	Incl. epoxy	Incl. core	Fitted experiment	
EI (Nm <sup>2</sup> )	Beam	1715.0	1778.3	1786.8	-	1195.8	49.4%
	Abaqus	1597.8	1565	1551.7	1704.4	1195.8	42.5%
	Difference	-6.8%	-12.0%	-13.2%	-		
EI* (Nm <sup>2</sup> )	Beam	1001.5	1070.3	1086.8	-	924.9	17.5%
	Abaqus	1051.0	1103.6	1099.2	1171.8	924.9	26.7%
	Difference	4.9%	3.1%	1.1%	-		
GJ (Nm <sup>2</sup> )	Beam	903.6	1058.8	1070.7	-	946.7	13.1%
	Abaqus	794.4	886.9	883.4	1013.3	946.7	7.0%
	Difference	-12.1%	-16.2%	-17.5%	-		
GJ* (Nm <sup>2</sup> )	Beam	527.7	637.2	651.3	-	732.2	-11.1%
	Abaqus	522.5	625.4	625.8	696.7	732.2	-4.9%
	Difference	-1.0%	-1.9%	-3.9%	-		
K (Nm <sup>2</sup> )	Beam	-802.9	-865.8	-865.7	-	-506.5	70.9%
	Abaqus	-659.1	-639.7	-632.2	-734.6	-506.5	45.1%
	Difference	-17.9%	-26.1%	-27.0%	-		
e (%c)	Beam	28.9	18.2	18.2	-	14.6%	3.6%c
	Abaqus	21.1	12.1	12.0	19.6	14.6%	5.0%c
	Difference	-7.9%c	-6.1%c	-6.2%c	-		

In order to investigate the source of the discrepancy between the beam model and the experimental wing in more detail and investigate the effect of the different skin regions and

the core on the cross-sectional properties, several finite element simulations were carried out in Abaqus, based on the updated airfoil shape shown in Fig. 13: (i) the skin using the fibre volume corrected properties, (ii) the skin including the leading edge strips, (iii), the skin including the leading edge strips and the epoxy, and (iv) the full model including the core. The resulting wing displacement and twist are shown in Fig. 8 and Fig. 9. For the sake of clarity, only the third and fourth Abaqus model are shown, since similar conclusions can be drawn from the results of the first and second model. The cross-sectional stiffness properties were determined by extracting the Abaqus deformations at 10 equally spaced spanwise locations on the wing and applying the same fitting procedure as used for the experimental results. The resulting cross-sectional stiffness properties are given in Table 9.

Based on the structural characterisation, several conclusions can be drawn. First, when comparing the updated beam results with the LE strips and epoxy to the corresponding Abaqus results, both results show good agreement in terms of wing displacement and wing twist, thus verifying the updated beam model. In case of wing twist, as expected, a slight offset is present caused by the warping restraint present in Abaqus, which is not accounted for in the beam model. When looking at the cross-sectional properties in Table 9, both models show significant differences. However, in case of wings that exhibit bend-twist coupling, care should be taken in interpreting these properties. As derived by Weisshaar,<sup>4</sup> the relation between applied bending moment and out-of-plane displacement, and applied torque and twist is no longer solely governed by bending stiffness and torsional stiffness, but also related to the bend-twist coupling, resulting in the following effective bending and torsional stiffnesses:

$$EI^* = EI \left( 1 - \frac{K^2}{EI GJ} \right) \quad (15)$$

$$GJ^* = GJ \left( 1 - \frac{K^2}{EI GJ} \right) \quad (16)$$

The resulting effective bending and torsional stiffnesses are also shown in Table 9 and show good to excellent agreement between the beam model and Abaqus. In order to investigate the discrepancies in the beam cross-sectional properties and the effect of the warping restraint on the equivalent beam properties in more detail, the beam cross-sectional properties of the Abaqus results for the first case (i.e. the skin using the fibre volume corrected properties) have been rederived excluding the effect of the warping restraint, by (i) only matching the region from 30% to 80% of the wing to remove the influence of the clamping region and load introduction region and (ii) matching the spanwise slope of deformation instead of the actual deformation values. The resulting wing cross-sectional properties are

**Table 10: Influence of the warping restraint on the beam cross-sectional properties**

Property	Present	Abaqus (Value fit)	Diff.	Abaqus (Slope fit)	Diff.
EI (Nm <sup>2</sup> )	1715.0	1597.8	-6.8%	1781.1	3.9%
EI* (Nm <sup>2</sup> )	1001.5	1051.0	4.9%	1044.7	4.3%
GJ (Nm <sup>2</sup> )	903.6	794.4	-12.1%	855.6	-5.3%
GJ* (Nm <sup>2</sup> )	527.7	522.5	-1.0%	501.9	-4.9%
K (Nm <sup>2</sup> )	802.9	659.1	-17.9%	793.8	-1.1%
e (%c)	28.9%	21.1%	-7.9%	30.2%	1.2%

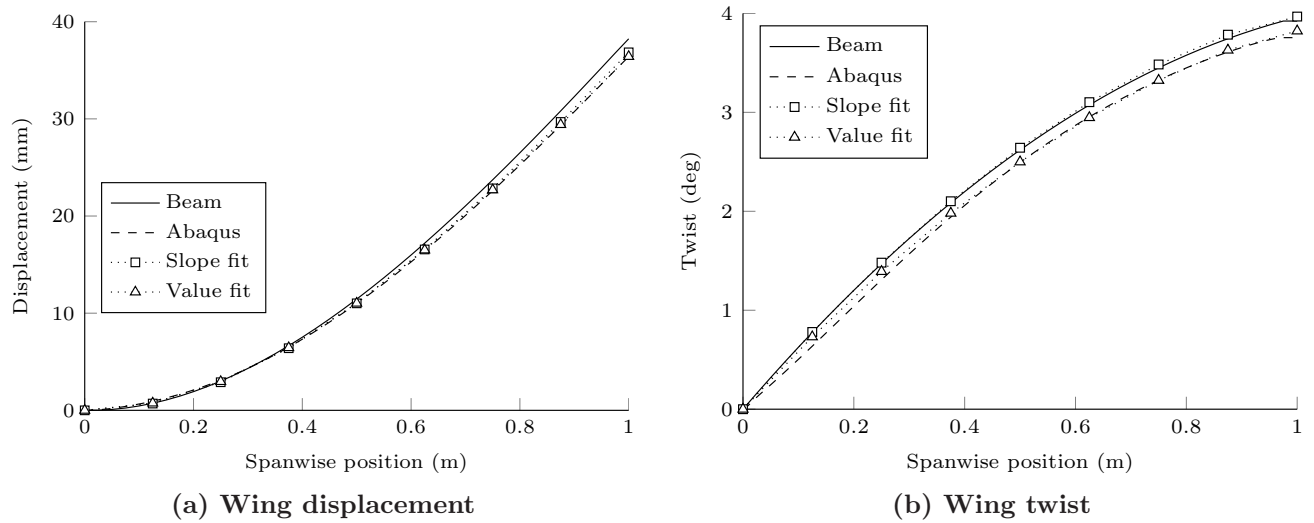


**Figure 14: Effect of the warping restraint on the beam deformations and the fitting procedure for the wing under a 10kg load at 97.5% span at the trailing edge**

given in Table 10 and an example of the corresponding wing deformations is shown in Fig. 14. As can be seen, when excluding the warping restraint, the cross-sectional properties of both models show good agreement, but in order to account for the effect of the warping restraint, as illustrated in Fig. 14, a redistribution of stiffness between the different equivalent beam properties occurs. The remaining differences in the beam stiffness properties are most likely related to the effect of inherent modelling differences between the beam model and the Abaqus shell model, such as cross-sectional deformations, on the equivalent beam properties. The influence of these effects on the aeroelastic response will be discussed in more detail when comparing the different numerical models to the wind tunnel test results.

Second, when comparing the numerical simulations and the experimental results, it can be concluded that good agreement is observed between the full model in Abaqus and the experimental results in terms of wing twist. In terms of wing displacement, excellent agree-

ment is also observed under an applied torque; however, both Abaqus and the beam model predict a lower wing displacement than observed in the experiment under an applied load. Possible causes for this mismatch could, for example, be uncertainties in material properties, slight variations in wing geometry, or slight flexibility in the clamp mechanism, introducing additional wing deflection in the experiments. As can be expected, these differences are also clearly reflected in the fitted beam properties shown in Table 9.

In conclusion, in comparing the experimental wing deformations to numerical simulations, several causes for discrepancies were found. A difference in ply thickness between the material test samples and the experimental wings, a deviation from the NACA0012 profile, and the strip in the leading edge for bonding both skins resulted in a first set of discrepancies. By accounting for these, excellent agreement is observed for the QI wing, thus providing a first validation of the numerical results. Secondly, by additionally accounting for the effect of the foam core, good agreement is also observed for the tailored wing.

In the remainder of this paper, the wind tunnel results will be investigated and the aeroelastic model will be validated using three sets of beam properties: (i) the properties from the cross-sectional modeller including leading strips and epoxy, (ii) the cross-sectional properties derived from the full Abaqus model, and (iii) the cross-sectional properties derived from the structural tests. Note that the cross-sectional modeller has been verified separately by Ferede and Abdalla<sup>30</sup> and is, therefore, not under investigation here.

## B. Wind tunnel test

All wings were tested at a range of free stream velocities from  $V = 10$  m/s up to  $V = 80$  m/s and at a range of incidence angles from  $\alpha = -10$  deg up to  $\alpha = 10$  deg. Due to the qualitatively similar behaviour only the results corresponding to  $V = 40$  m/s,  $V = 60$  m/s and  $V = 80$  m/s are presented. The experimental wind tunnel results are compared to three sets of beam properties: (i) the properties from the cross-sectional modeller including leading strips and epoxy to validate the beam model, (ii) the cross-sectional properties derived from the full Abaqus model to investigate the effect of the core and the warping restraint at the root, and (iii) the fitted properties derived from the structural tests to validate the aeroelastic simulations.

### 1. Lift and root bending moment coefficient

A comparison between the numerical beam results and the experimental results for the lift and root bending moment coefficient of the QI wing are shown in Fig. 15 and Fig. 16. In case of lift, the numerical and experimental results show good agreement with a slightly higher predicted lift curve slope than measured in the experiment. At angles of attack larger

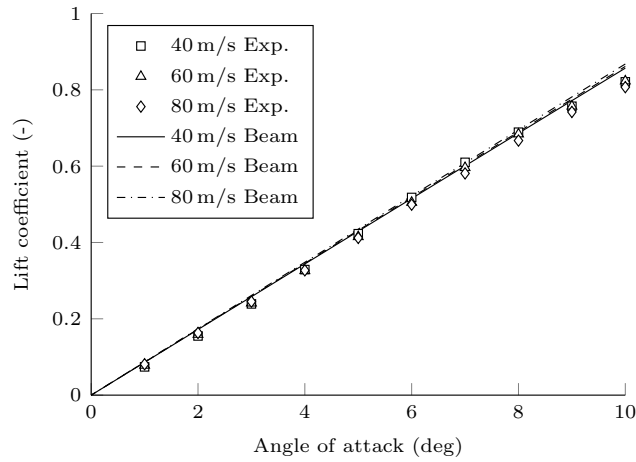


Figure 15: Lift coefficient of the QI wing

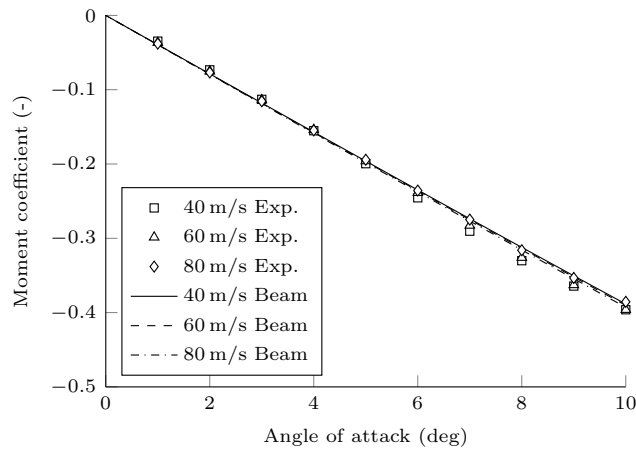


Figure 16: Root bending moment coefficient of the QI wing

than 8 deg slight non-linearity is observed in the measurements, most likely related to the onset of stall on the wing. Excluding the results with aerodynamic nonlinearities, which are not captured by the present simulations, the error ranges from 0.5% to 4.6%. In the case of the root bending moment, the numerical results show excellent agreement with the experimental results with an error ranging from 0.5% to 3.8%.

Fig. 17 and Fig. 18 show the lift coefficient and root bending moment coefficient comparisons for the tailored wing. First of all, it is interesting to note that, the differences between the fitted properties obtained from the structural tests, the cross-sectional properties derived from the full Abaqus model, and the beam model including LE strips and epoxy are negligible, thus showing that the effect of the core and the warping restraint on the aeroelastic loads can be neglected. Secondly, it can be concluded that, in terms of lift, the numerical results show excellent agreement to the experimental results with an error ranging from 0.2% to 4.7%. However, in terms of root bending moment coefficient, especially at 40 m/s and 60 m/s, and high angles of attack, the numerical results predict a slightly lower root bending

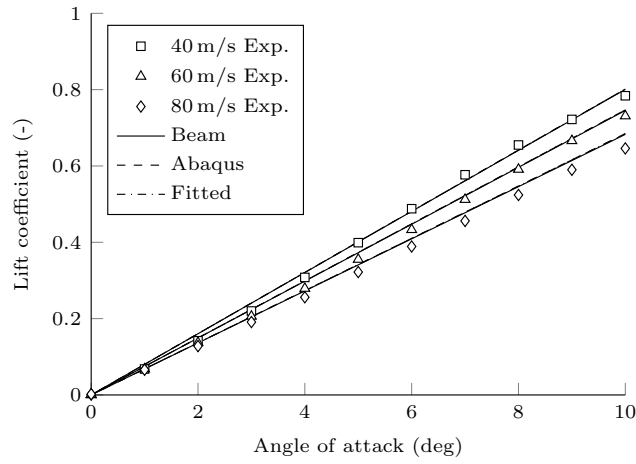


Figure 17: Lift coefficient of the tailored wing

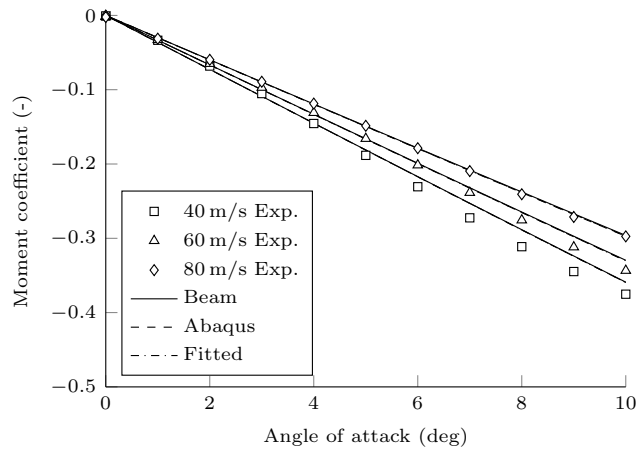
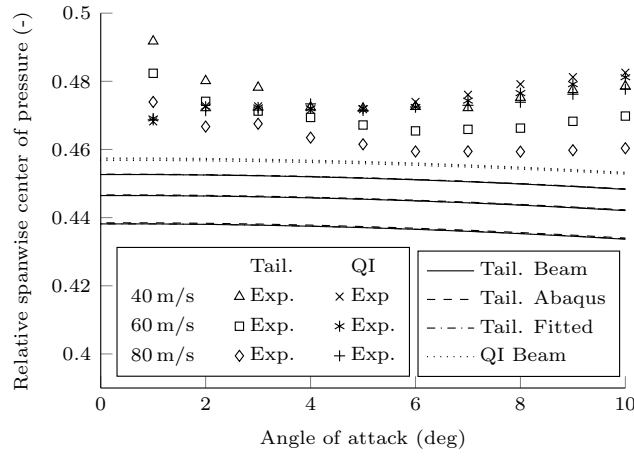


Figure 18: Root bending moment coefficient of the tailored wing

moment coefficient than observed in the experiments with an error ranging from 1.2% to 7.5%.

In order to compare the two wings and investigate the effect of load alleviation, an important parameter is the spanwise location of the center of pressure of the wing shown in Fig. 19, which has been obtained by dividing the root bending moment coefficient by the lift coefficient. From this figure, several conclusions can be drawn. First, both the experimental results and the numerical simulations show that the QI wing does not alleviate loads due to the lack of bend-twist coupling and a shear center location of 23% chord, which is close to the quarter chord center of pressure. The difference of up to 2.5% span between the numerical simulations and the experimental results is considered good agreement and can be explained by, for example, manufacturing quality and assumptions made in the simulations.

Secondly, the tailored wing clearly shows load alleviation by shifting the center of pressure inboard as the velocity is increased. Similar to the QI wing, a difference is observed between the numerical simulations and the experimental results. It is interesting to note



**Figure 19: Location of the spanwise center of pressure for the QI and tailored wing at different velocities**

that, although there is a difference between the numerical simulations and the experimental results, the relative shift in center of pressure as the velocity increases shows excellent agreement, especially at higher angles of attack.

Finally, when comparing the tailored wing and the QI wing, the experimental results show less load alleviation than expected from the numerical simulations. This is most likely caused by slight geometrical differences between both wings.

It is interesting to note that manoeuvre load alleviation is almost independent of the angle of attack. For a symmetric wing without pre-twist, given a certain velocity, this can be explained by the fact that both the aerodynamic loads and the wing twist start from zero and are linear with respect to the angle of attack. Therefore, given a lift distribution for, for example, an angle of attack of 1 deg, doubling the angle of attack to 2 deg will double the resulting lift and wing twist; however, since both effects are linear, the resulting lift distribution is almost unaffected. However, a change in air speed does affect the lift distribution, as the aerodynamic loads are quadratic in air speed and, thus, for the same lift generated a different wing twist distribution and, consequently, lift distribution is obtained.

In conclusion, when including the effects of the fibre volume corrected properties, LE strip, and epoxy, the beam results show good agreement with the experimental results, thus validating the loads predicted by the aeroelastic analysis framework.

## 2. Wing deformation

Fig. 20 and Fig. 21 show the comparison of the wing tip deflection and wing tip twist between the DIC measurements, the optical marker tracking system (Photo) and the numerical beam simulations for the QI wing. The wing deflection and wing twist results show good agreement for 40 m/s and 60 m/s with errors ranging from 1.0% to 7.5% for deflection and

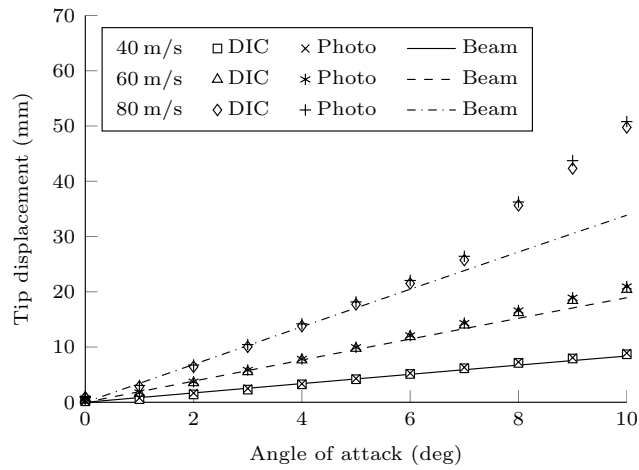


Figure 20: Out-of-plane tip deflection of the QI wing at different velocities

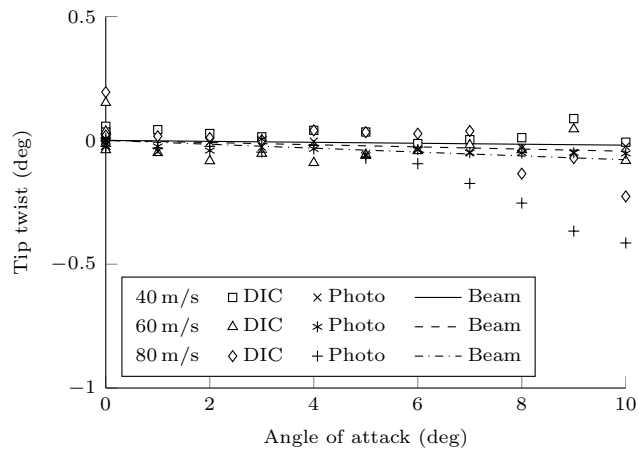


Figure 21: Tip twist of the QI wing at different velocities

up to 0.1 deg for twist. At 80 m/s and an angle of attack larger than 7 deg the wing buckled, resulting in differences between the experimental results and the numerical simulations. Fig. 22 and Fig. 23 show the out-of-plane displacement and twist distribution along the span at an angle of attack of 10 deg. At 40 m/s and 60 m/s, the experimental results and the numerical simulations show good agreement, however, at 80 m/s the wing buckled and thus the results clearly differ. Note that the experimental wing twist is derived from the displacement measurements which is why close to the wing root, the experimental results show a small wing twist due to measurement inaccuracies, while the simulations predict almost no wing twist.

The comparison of the wing tip deflection and tip twist between the different measurement techniques and the numerical simulations for the tailored wing is shown in Fig. 24 and Fig. 25. Similar to the results from the structural tests, the beam model including LE strips and epoxy and the full Abaqus model predict a stiffer wing in bending than obtained from

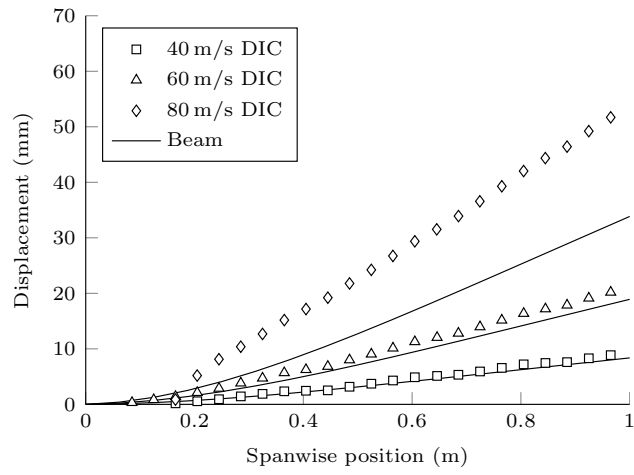


Figure 22: Out-of-plane deflection of the quarter-chord line of the QI wing at  $\alpha = 10$  deg

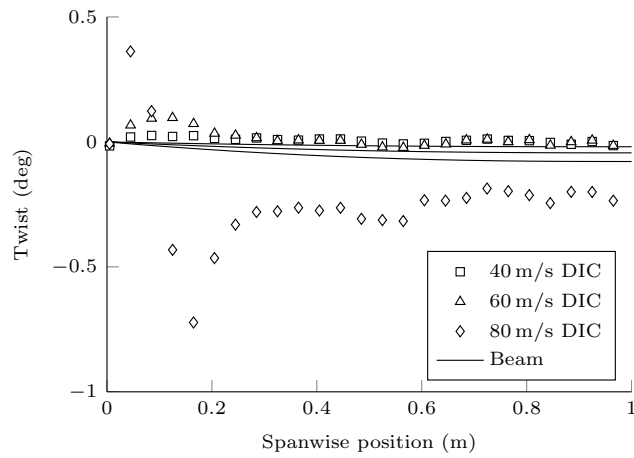
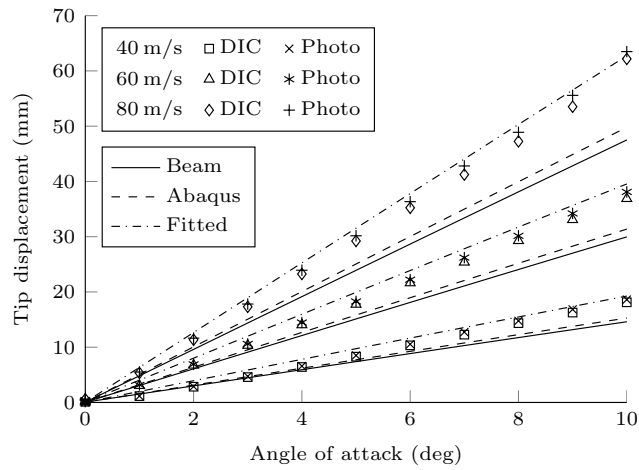


Figure 23: Twist of the QI wing at  $\alpha = 10$  deg



**Figure 24: Out-of-plane tip deflection of the tailored wing at different velocities**

the experimental results with errors ranging from 10% to 22% for the beam model and 7% to 19% for the Abaqus model. When looking at the wing twist, it is interesting to note that, even though all models have different cross-sectional properties, the difference in the resulting twist distribution under aerodynamic loads is negligible, showing that the effect of the core and warping restraint on the aeroelastic twist is negligible. When comparing the beam twist results to the experimental twist results, the beam results predict a tip twist which is 4% to 10% higher, which is consistent with the larger load alleviation observed in the root bending moment results.

The out-of-plane displacement and twist distribution along the span at an angle of attack of 10 deg are shown in Fig. 26 and Fig. 27. Similar to the QI wing, at 40 m/s and 60 m/s the experimental wing displacement and the numerical simulations using the fitted cross-sectional properties show excellent agreement, however at 80 m/s the wing buckled and thus the results clearly differ. It is interesting to note that, while the tip deflection is clearly affected by buckling, the wing twist is much less affected. As also observed in the structural tests, the beam and Abaqus simulations predict a stiffer wing in bending than the experimental results. When looking at the wing twist, as already concluded from the tip twist results, the numerical simulations predict a slightly higher wing twist than observed in the experiment.

Comparing the QI wing to the tailored wing, first of all, it can be seen that, as expected, the tailored wing alleviates loads by a wash-out deformation, while the QI wing does not due to the lack of bend-twist coupling and a shear center location of 23% chord, which is close to the quarter chord center of pressure. Second of all, it is interesting to note that the QI wing buckled at a lower angle of attack than the tailored wing, even though its skin is thicker. This can be explained by two effects: (i) the tailored wing alleviates loads and thus the actual force and bending moment on the wing is smaller and (ii) the tailored wing skins

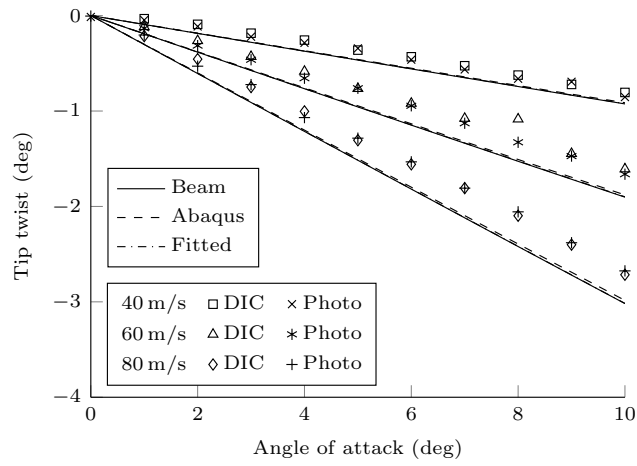


Figure 25: Tip twist of the tailored wing at different velocities

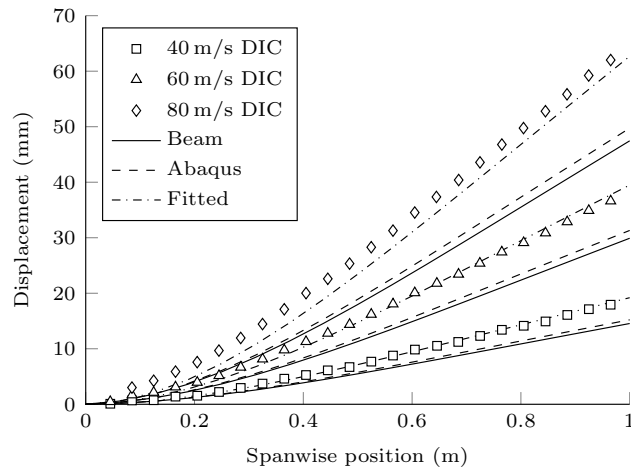


Figure 26: Out-of-plane deflection of the quarter-chord line of the tailored wing at  $\alpha = 10$  deg

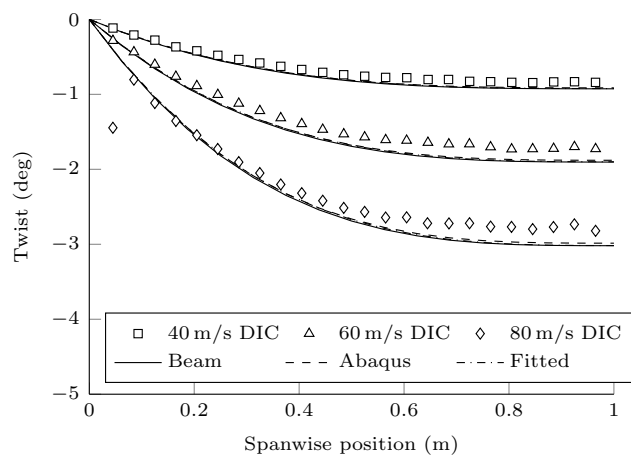


Figure 27: Twist of the tailored wing at  $\alpha = 10$  deg

are supported by a foam core over the entire surface, while the wing skins of the QI wing are only reinforced by foam ribs at discrete locations.

In conclusion, although the error in wing deflection of the tailored wing ranges from 10% to 22%, the wind tunnel results show reasonable to good agreement to the aeroelastic beam simulations, in terms of wing twist with errors ranging from 4% to 10%, in terms of predicted loads with errors ranging from 0.2% to 7.5%, and in terms of wing deflection for the QI wing with errors ranging from 1.0% to 7.5%, thus validating the aeroelastic analysis framework. Possible causes for the discrepancies in wing deflection of the tailored wing are slight variations in material properties or wing geometry, or some flexibility in the clamping mechanism resulting in additional wing deflection in the experiments. Furthermore, the results obtained using the cross-sectional properties derived from the Abaqus model show that the effect of the core and warping restraint on the aeroelastic response is negligible.

## VII. Conclusion

The goal of the present paper was to provide experimental validation data for composite aeroelastically tailored wings with a closed-cell cross-sectional structure and in the process validate the aeroelastic analysis framework developed at the Delft University of Technology. The framework has been used for the design of several aeroelastically tailored wings designed to alleviate loads. Based on the optimisation results, three wings were manufactured: (i) a 6 layer quasi-isotropic wing to act as reference, (ii) a 3 layer constant stiffness tailored wing, and (iii) a 4 layer constant stiffness tailored wing.

Structural tests were carried out, rendering the 3 layer tailored wing unsuitable for wind tunnel tests due to buckling. However, the 6 layer quasi-isotropic wing and the 4 layer tailored wing were successfully tested, both structurally and in the wind tunnel. During the wind tunnel tests, the aerodynamic forces and moments have been measured using a six component balance, a digital image correlation system has been used to measure the wing deformation and an optical marker tracking system has been used to measure the tip deflection and tip twist. The wings have been tested at a range of angles of attack up to a flight speed of 80 m/s.

The experimental data has been compared to the numerical simulations showing good agreement for the quasi-isotropic wing, both in terms of wing deformations with errors in the range of 1.0% to 7.5% and in terms of predicted loads with errors ranging from 0.5% to 4.6%. In case of the 4 layer tailored wing discrepancies were still observed in the wing deflection with errors in the range of 10% to 22%, even after accounting for the LE strip connecting the two wing halves and the epoxy used to glue in the core. However, reasonable to good agreement is observed in terms of wing twist with errors in the range of 4% to 10%

and predicted loads with errors in the range of 0.2% to 7.5%.

The effect of the foam core and the warping restraint at the wing root, which are not accounted for in the beam model, on the aeroelastic response has been assessed by using cross-sectional properties derived from Abaqus simulations of the complete wing, showing that effects had negligible influence on the aeroelastic response.

In conclusion, structural tests and wind tunnel tests have been successfully performed on aeroelastically tailored wings; first of all, providing experimental validation data for composite aeroelastically tailored wings and, second of all, validating the aeroelastic analysis and design framework developed at the Delft University of Technology.

## Acknowledgments

The authors would like to thank Peter Loeffen for his help with manufacturing and preliminary structural testing.

## References

- <sup>1</sup>Shirk, M. H., Hertz, T. J., and Weisshaar, T. A., "Aeroelastic Tailoring Theory, Practice, and Promise," *Journal of Aircraft*, Vol. 23, No. 1, 1986, pp. 6–18.
- <sup>2</sup>Qin, Z. M., Marzocca, P., and Librescu, L., "Aeroelastic instability and response of advanced aircraft wings at subsonic flight speeds," *Aerospace Science and Technology*, Vol. 6, 2002, pp. 195–208.
- <sup>3</sup>Qin, Z. M., Librescu, L., and Marzocca, P., "Aeroelasticity of composite aerovehicle wings in supersonic flows," *Journal of Spacecraft and Rockets*, Vol. 40, No. 2, 2003, pp. 162–173.
- <sup>4</sup>Weisshaar, T. A., "Aeroelastic Tailoring - Creative uses of unusual materials," *Proceedings of 28th Structures, Structural Dynamics and Materials Conference*, 1987.
- <sup>5</sup>Danilin, A. I. and Weisshaar, T. A., "The use of structural optimality criteria for aircraft conceptual design," *Proceedings of 41st AIAA/ASME/ASCE/AHS/ASC Structures, Structural Dynamics and Materials Conference*, 2000.
- <sup>6</sup>Livne, E. and Weisshaar, T. A., "Aeroelasticity of nonconventional airplane configurations - Past and future," *Journal of Aircraft*, Vol. 40, No. 6, 2003, pp. 1047–1065.
- <sup>7</sup>Weisshaar, T. A. and Duke, D. K., "Induced drag reduction using aeroelastic tailoring with adaptive control surfaces," *Journal of Aircraft*, Vol. 43, No. 1, 2006, pp. 157–164.
- <sup>8</sup>Eastep, F. E., Tischler, V. A., Venkayya, V. B., and Khot, N. S., "Aeroelastic Tailoring of Composite Structures," *Journal of Aircraft*, Vol. 36, No. 6, 1999, pp. 1041–1047.
- <sup>9</sup>Arizono, H. and Isogai, K., "Application of genetic algorithm for aeroelastic tailoring of a cranked-arrow wing," *Journal of Aircraft*, Vol. 42, No. 2, 2005, pp. 493–499.
- <sup>10</sup>Guo, S. J., Bannerjee, J. R., and Cheung, C. W., "The effect of laminate lay-up on the flutter speed of composite wings," *Proceedings of the Institution of Mechanical Engineers Part G: Journal of Aerospace Engineering*, Vol. 217, No. G3, 2003, pp. 115–122.

- <sup>11</sup>Dillinger, J. K. S., Klimmek, T., Abdalla, M. M., and Gürdal, Z., “Stiffness Optimization of Composite Wings with Aeroelastic Constraints,” *Journal of Aircraft*, Vol. 50, No. 4, 2013, pp. 1159–1168.
- <sup>12</sup>Guo, S. J., Cheng, W. Y., and Cui, D. G., “Aeroelastic tailoring of composite wing structures by laminate layup optimization,” *AIAA Journal*, Vol. 44, No. 12, 2006, pp. 3146–3150.
- <sup>13</sup>Kameyama, M. and Fukunaga, H., “Optimum design of composite plate wings for aeroelastic characteristics using lamination parameters,” *Computers & Structures*, Vol. 85, No. 3-4, 2007, pp. 213–224.
- <sup>14</sup>Manan, A., Vio, G. A., Harmin, M. Y., and Cooper, J. E., “Optimization of aeroelastic composite structures using evolutionary algorithms,” *Engineering Optimization*, Vol. 42, No. 2, 2010, pp. 171–184.
- <sup>15</sup>De Leon, D. M., de Souza, C. E., Fonseca, J. S. O., and da Silva, R. G. A., “Aeroelastic tailoring using fiber orientation and topology optimization,” *Structural and Multidisciplinary Optimization*, Vol. 46, No. 5, 2012, pp. 663–677.
- <sup>16</sup>Kim, T. U. and Hwang, I. H., “Optimal design of composite wing subjected to gust loads,” *Computers & Structures*, Vol. 83, No. 19-20, 2005, pp. 1546–1554.
- <sup>17</sup>Stodieck, O., Cooper, J. E., Weaver, P. M., and Kealy, P., “Improved aeroelastic tailoring using tow-steered composites,” *Composite Structures*, Vol. 106, 2013, pp. 703–715.
- <sup>18</sup>Stanford, B. K., Jutte, C. V., and Chauncey Wu, K., “Aeroelastic benefits of tow steering for composite plates,” *Composite Structures*, Vol. 118, 2014, pp. 416–422.
- <sup>19</sup>Stanford, B. K., Jutte, C. V., and Wieseman, C. D., “Trim and Structural Optimization of Subsonic Transport Wings Using Nonconventional Aeroelastic Tailoring,” *AIAA Journal*, Vol. 54, No. 1, 2016, pp. 293–309.
- <sup>20</sup>Brooks, T. R., Kennedy, G., and Martins, J., “High-fidelity Aerostructural Optimization of a High Aspect Ratio Tow-steered Wing,” *57th AIAA/ASCE/AHS/ASC Structures, Structural Dynamics, and Materials Conference*, 2016.
- <sup>21</sup>Kennedy, G. J., Kenway, G. K. W., and Martins, J. R. R., “A Comparison of Metallic, Composite and Nanocomposite Optimal Transonic Transport Wings,” Tech. Rep. NASA CR-2014-0218185, 2014.
- <sup>22</sup>Thuwis, G. A. A., Breuker, R., Abdalla, M. M., and Gürdal, Z., “Aeroelastic tailoring using lamination parameters,” *Structural and Multidisciplinary Optimization*, Vol. 41, No. 4, 2009, pp. 637–646.
- <sup>23</sup>Sherrer, V. C., Hertz, T. J., and Shirk, M. H., “Wind Tunnel Demonstration of Aeroelastic Tailoring Applied to Forward Swept Wings,” *Journal of Aircraft*, Vol. 18, No. 11, 1981, pp. 976–983.
- <sup>24</sup>Blair, M. and Weisshaar, T. A., “Swept Composite Wing Aeroelastic Divergence Experiments,” *Journal of Aircraft*, Vol. 19, No. 11, 1982, pp. 1019–1024.
- <sup>25</sup>Hollowell, S. J. and Dugundji, J., “Aeroelastic flutter and divergence of stiffness coupled, graphite/epoxy cantilevered plates,” *Journal of Aircraft*, Vol. 21, No. 1, 1984, pp. 69–76.
- <sup>26</sup>Landsberger, B. J. and Dugundji, J., “Experimental aeroelastic behavior of unswept and forward-swept cantilever graphite/epoxy wings,” *Journal of Aircraft*, Vol. 22, No. 8, 1985, pp. 679–686.
- <sup>27</sup>Chen, G.-S. and Dugundji, J., “Experimental aeroelastic behavior of forward-swept graphite/epoxy wings with rigid-body freedom,” *Journal of Aircraft*, Vol. 24, No. 7, 1987, pp. 454–462.
- <sup>28</sup>Werter, N. P. M. and De Breuker, R., “Aeroelastic Tailoring and Structural Optimisation Using an Advanced Dynamic Aeroelastic Framework,” *Proceedings of the International Forum on Aeroelasticity and Structural Dynamics 2015*, St. Petersburg, Russia, 2015.
- <sup>29</sup>Tsai, S. and Pagano, N., “Invariant Properties of Composite Materials,” *Composite Materials Workshop*, Technomic Publishing Co., Westport, 1968, pp. 233–253.

<sup>30</sup>Ferede, E. and Abdalla, M. M., “Cross-sectional modelling of thin-walled composite beams,” *Proceedings of 55th AIAA/ASME/ASCE/AHS/SC Structures, Structural Dynamics, and Materials Conference*, American Institute of Aeronautics and Astronautics, 2014.

<sup>31</sup>Hammer, V., Bendse, M., Lipton, R., and Pedersen, P., “Parametrization in laminate design for optimal compliance,” *International Journal of Solids and Structures*, Vol. 34, No. 4, 1997, pp. 415–434.

<sup>32</sup>Svanberg, “A class of globally convergent optimization methods based on conservative convex separable approximations,” *SIAM Journal on Optimization*, Vol. 12, No. 2, 2002, pp. 555–573.

<sup>33</sup>Correlated Solutions, Inc., “VIC-3D™ Measurement System,” 2015.

<sup>34</sup>Micro Epsilon, “optoNCDT 1302 Compact laser sensor,” 2015.

<sup>35</sup>Daniel, I. M. and Ishai, O., *Engineering Mechanics of Composite Materials*, Oxford University Press, New York, 2006.